


Random vibration energy harvesting on thin plates using multiple piezopatches

Journal of Intelligent Material Systems and Structures
2016, Vol. 27(20) 2744–2756
© The Author(s) 2016
Reprints and permissions:
sagepub.co.uk/journalsPermissions.nav
DOI: 10.1177/1045389X16635846
jim.sagepub.com


Ugur Aridogan¹, Ipek Basdogan¹ and Alper Erturk²

Abstract

Vibrational energy harvesting using piezoelectric cantilever beams has received significant attention over the past decade. When compared to piezoelectric cantilever-based harvesters, piezopatch energy harvesters integrated on plate-like thin structures can be a more efficient and compact option to supply electrical power for wireless structural health and condition monitoring systems. In this article, electroelastic modeling, analytical and numerical solutions, and experimental validations of piezopatch-based energy harvesting from stationary random vibrations of thin plates are presented. Electroelastic models for the series and parallel connected multiple piezopatches are given based on a distributed-parameter modeling approach for a thin host plate excited by a transverse point force. The analytical and numerical solutions for the mean power output and the mean-square shunted vibration response are then derived. The experimental measurements are carried out by employing a fully clamped thin plate with three piezopatches connected in series. It is shown that the analytical and numerical model predictions for the mean power output and the mean-square velocity response are in very good agreement with the experimental measurements. The electroelastic modeling framework and solution methods presented in this work can be used for design, performance analysis, and optimization of piezoelectric energy harvesting from stationary random vibration of thin plates.

Keywords

energy harvesting, piezoelectricity, plates, vibration

Introduction

Research in vibrational energy harvesting has received growing attention over the past decade (Anton and Sodano, 2007; Beeby et al., 2006; Cook-Chennault et al., 2008). The ultimate goal of this research area is to enable self-powered electronic devices and eliminate the need of battery replacement and disposal (Anton and Sodano, 2007; Beeby et al., 2006). In the existing literature, a wide variety of vibrational energy harvesting systems has been developed using fundamental transduction principles (e.g. electrostatics (Lee et al., 2009), electromagnetism (Beeby et al., 2007; Elliott and Zilletti, 2014), piezoelectricity (Erturk and Inman, 2011)), and alternative conversion techniques (e.g. magnetostriction (Wang and Yuan, 2008) and use of ionic polymers (Tiwari and Kim, 2013)). Among these conversion alternatives, piezoelectric energy harvesting has received most of the attention because of its wide range of applicability, relatively mature fabrication methods at different geometric scales, and high power density (Cook-Chennault et al., 2008).

Cantilevered beam-based piezoelectric harvesters (e.g. unimorphs and bimorphs) have been arguably the most commonly considered forms of piezoelectric energy harvesters. Electromechanically coupled analytical (Erturk and Inman, 2008), semi-analytical (Erturk, 2012), and finite element (Elvin and Elvin, 2009; Yang and Tang, 2009) models have been developed, and experimental investigations have been reported for harmonic (Erturk and Inman, 2009) and random (Zhao and Erturk, 2013a) base excitations. It is well-known that the power generation performance of a linear resonant harvester beam depends on how well the

¹Department of Mechanical Engineering, College of Engineering, Koç University, Istanbul, Turkey

²George W. Woodruff School of Mechanical Engineering, Georgia Institute of Technology, Atlanta, GA, USA

Corresponding author:

Ipek Basdogan, Department of Mechanical Engineering, College of Engineering, Koç University, 34450 Istanbul, Turkey.
Email: ibasdogan@ku.edu.tr

dominant ambient frequency matches with its fundamental resonance frequency due to the narrow bandwidth around the fundamental resonance frequency (Tang et al., 2010). Therefore, performance enhancement of cantilevered beam harvesters has been widely studied with different design configurations for broadband base excitations (Erturk et al., 2009; Ferrari et al., 2008; Friswell and Adhikari, 2010; Huan et al., 2008; Huang and Lin, 2012; Lien and Shu, 2012).

In many real-life applications, ambient mechanical energy is distributed over a broad frequency spectrum and it often exhibits stochastic characteristics. However, as opposed to the large amount of research on harmonic excitation (Tang et al., 2010), limited research has been conducted for non-harmonic or random excitations of resonant harvesters. Random vibration energy harvesting has been studied with lumped-parameter (Adhikari et al., 2009; Barton et al., 2010; Blystad et al., 2010; Ferrari et al., 2009; Scruggs, 2009; Tvedt et al., 2010) and distributed-parameter (Zhao and Erturk, 2013a) modeling, while nonlinear structures with higher complexities, such as Duffing oscillators, have been modeled and analyzed by others (Daqaq, 2010, 2011; Kumar et al., 2014; Litak et al., 2010; Ramlan et al., 2010; Zhao and Erturk, 2013b) in parallel.

Piezopatch-based energy harvesting is a compact and practical method especially for light-weight, thin, and two-dimensional structures since harvester patches can be implemented without modifying the host structure's dynamics. Recently, an analytical model of a single patch-based energy harvester was presented for vibrations of thin plates by Aridogan et al. (2014a). Electromechanical finite element model of piezoelectric energy harvester plates was presented by De Marqui et al. (2009) and extended for electroaeroelastic problems (De Marqui and Erturk, 2012; De Marqui et al., 2011). Topology optimizations using finite element models were carried out by Rupp et al. (2009) and Lee and Youn (2011) in order to increase the efficiency of the piezoelectric layers attached on plate-like structures.

It is worth mentioning that prior to, and in parallel with, energy harvesting research on plate-like structures, some groups have focused on passive damping of plate vibrations using piezoelectric shunt damping (Moheimani, 2003). Piezoelectric shunt damping of plate-like structures was studied for vibration suppression (Behrens et al., 2003; Kim and Jung, 2006; Kim and Kwak, 2004; Koshigoe and Murdock, 1993; Moheimani, 2003; Moheimani and Behrens, 2004; Niederberger et al., 2004; Saravanos, 1999) and structure-borne noise attenuation (Casadei et al., 2010; Kim and Jung, 2006; Kim and Kim, 2004). As a relatively recent trend, hybrid mechanisms employing piezoelectric energy harvesting and shunt damping together were considered to develop self-powered vibration control systems (Lallart et al., 2009; Makihara

et al., 2012; Takeuchi et al., 2012). More recently, a piezoelectric corrugated device for concurrent vibration suppression and energy harvesting was modeled, manufactured, and tested by Harne (2012). The corrugated device includes a distributed piezoelectric spring layer below a top plate and can be attached on a plate-like host structure (Harne and Fuller, 2012). Performance of the corrugated device for vibration suppression and energy harvesting was investigated by attaching it on a simply supported plate (Harne, 2012) and on a structural panel of a typical bus (Harne, 2013) under the effect of harmonic vibrations.

In this article, piezopatch-based energy harvesting from random vibrations of thin plates is presented with electroelastic modeling, frequency-domain and time-domain solutions, as well as experimental investigations. In the following, electroelastic models for the series and parallel connection cases of piezopatches are given based on a distributed-parameter modeling approach, which are then employed in deterministic and band-limited random vibrations of a thin host plate. For stationary random vibrations, the frequency-domain analytical solutions of the mean power output and mean-square vibration response are expressed based on electroelastic frequency response functions (FRFs) and the power spectral density (PSD) of the force input. Time-based numerical solutions are obtained in the first-order representation in a deterministic fashion by considering the Fourier series expansion of the force input. Finally, experimental case studies are presented to validate the frequency-domain and time-domain solutions for a wide range of resistive loads.

Distributed-parameter electroelastic model

Electromechanically coupled mechanical equation of host plate vibrations

Figure 1(a) and (b), respectively, illustrates the series and parallel connection configurations of piezopatch energy harvesters structurally integrated on a thin host plate, which is excited by a transverse point force $f(t)$ at position (x_0, y_0) and time t . Piezopatch energy harvesters are in the form of transversely isotropic thin piezoceramic sheets with two opposite corners located at $(x_{k,1}, y_{k,1})$ and $(x_{k,2}, y_{k,2})$ for $k = 1, 2, \dots, K$, where K is the number of the piezopatch harvesters. The bottom and top surfaces of the piezopatch harvesters are assumed to be covered by highly conductive and negligibly thin electrode layers. A load resistance R_l is considered as an electrical load connected to the resultant terminals of the series and parallel configurations. It is assumed that the force excitation is persistent, thus the voltage output, $v(t)$, across the load resistance can be continuously extracted.

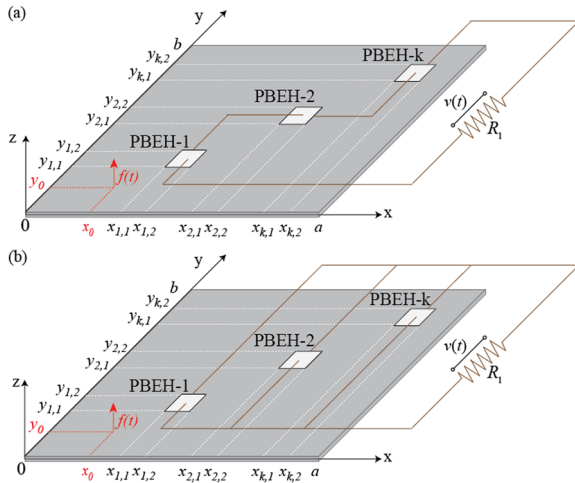


Figure 1. Schematics of piezopatch energy harvesters on a thin plate: (a) series and (b) parallel connection configurations.

The forced linear vibration of a thin plate accounting for the electromechanical coupling due to thin piezopatch energy harvesters is governed by (Aridogan et al., 2014a)

$$\begin{aligned}
 & D \left(\frac{\partial^4 w(x, y, t)}{\partial x^4} + 2 \frac{\partial^4 w(x, y, t)}{\partial x^2 \partial y^2} + \frac{\partial^4 w(x, y, t)}{\partial y^4} \right) \\
 & + c \frac{\partial w(x, y, t)}{\partial t} + m \frac{\partial^2 w(x, y, t)}{\partial t^2} \\
 & - \sum_{k=1}^K \theta_k v_k(t) \left\{ \left[\frac{d\delta(x - x_{k,1})}{dx} - \frac{d\delta(x - x_{k,2})}{dx} \right] \right. \\
 & [H(y - y_{k,1}) - H(y - y_{k,2})] \\
 & + \left. \left[\frac{d\delta(y - y_{k,1})}{dy} - \frac{d\delta(y - y_{k,2})}{dy} \right] \right\} \\
 & [H(x - x_{k,1}) - H(x - x_{k,2})] \Big\} = f(t) \delta(x - x_0) \delta(y - y_0)
 \end{aligned} \tag{1}$$

where $w(x, y, t)$ is the transverse displacement of the reference (neutral) surface at an arbitrary position (x, y) of the plate and at time t . The voltage across the electrodes (i.e. individual voltage output) of the k th piezopatch is denoted by $v_k(t)$. The thickness of the plate (h) is assumed to be uniform and much smaller than the length a and the width b of the plate to justify the assumptions of Kirchhoff's thin plate theory. The flexural rigidity of the plate is given by $D = Yh^3 / (12 - 12\nu^2)$, where Y is the Young's modulus and ν is the Poisson's ratio under short-circuit conditions. The mass per unit area of the plate and the viscous damping coefficient are denoted by m and c , respectively. $H(x)$ and $H(y)$ are the Heaviside functions, and $\delta(x)$ and $\delta(y)$ are the Dirac delta functions along the x - and y -axes, respectively. Assuming that the total

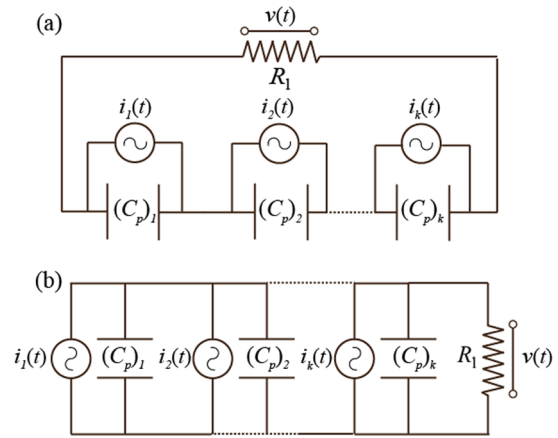


Figure 2. Electrical circuits of piezopatch harvesters connected to a resistive load: (a) series and (b) parallel connection configurations (current sources depend on the voltage output due to backward coupling).

volume of the piezopatches is much smaller than that of the host plate, added mass and bending stiffness contributions of the patches are neglected. However, the electromechanical coupling between the piezopatch energy harvesters and the thin plate is taken into account in equation (1) due to the converse piezoelectric effect. The electromechanical coupling term θ_k for the k th piezopatch is $\theta_k = (\bar{e}_{31})_k (h_{pc})_k \tau_k$, where $(\bar{e}_{31})_k$ is the effective plane-stress piezoelectric constant, $(h_{pc})_k$ is the reference distance between the neutral surface of the plate and the center of the piezopatch along the z -axis, and τ_k is the polarity constant used for the forward and reverse connections of the electrodes in wiring (i.e. τ_k equals to either $+1$ for the forward manner or -1 for the reverse manner connection of electrode layers).

Coupled electrical circuit equations for series and parallel connections

Figure 2 shows electrical circuit representations for the series and parallel connection configurations of the piezopatch harvesters. In the electrical circuit analysis, the piezopatch harvesters are modeled as dependent current sources in parallel with their internal capacitances.

For the series connection configuration presented in Figure 2(a), the voltage output $v(t)$ across the resistive load is the sum of the individual voltage outputs $v_k(t)$ of the piezopatch harvesters connected in series, that is, $v(t) = \sum_{k=1}^K v_k(t)$. Applying Kirchhoff's circuit laws, the governing electrical circuit equation for the k th piezopatch can be written as (Aridogan et al., 2014b)

$$(C_p)_k \frac{dv_k(t)}{dt} + \sum_{k=1}^K \frac{v_k(t)}{R_1} = i_k(t) \quad k = 1, 2, \dots, K \tag{2}$$

where $i_k(t)$ and $(C_p)_k$ are the dependent current output of the k th piezopatch and its internal capacitance, respectively, which are given by

$$i_k(t) = -\theta_k \left\{ \int_{y_{k,1}}^{y_{k,2}} \int_{x_{k,1}}^{x_{k,2}} \left[\frac{\partial^3 w(x,y,t)}{\partial x^2 \partial t} + \frac{\partial^3 w(x,y,t)}{\partial y^2 \partial t} \right] dx dy \right\}$$

$$(C_p)_k = (\bar{\epsilon}_{33}^S)_k \frac{(l_p)_k (w_p)_k}{(h_p)_k} \quad (3)$$

where $(l_p)_k$, $(w_p)_k$, and $(h_p)_k$ are the length, width, and thickness of the k th piezopatch, respectively, and $(\bar{\epsilon}_{33}^S)_k$ is the permittivity of the k th patch at constant strain in plane-stress conditions. Note that the number of governing circuit equations is equal to the number of piezopatches connected in series.

For the case of parallel connection illustrated in Figure 2(b), the individual voltage output of each k th piezopatch is equal to the voltage across the resistive load, that is, $v(t) = v_k(t)$. Thus, the electrical dynamics of the parallel configuration is governed by only one circuit equation given as follows (Aridogan et al., 2014b)

$$\frac{dv(t)}{dt} \sum_{k=1}^K (C_p)_k + \frac{v(t)}{R_l} = \sum_{k=1}^K i_k(t) \quad (4)$$

where $(C_p)_k$ and $i_k(t)$ are given by equation (3). Therefore, equations (1) and (2) govern the coupled electroelastic dynamics of harvesters connected in series, while equations (1) and (4) describe the governing dynamics for parallel connection.

Governing electroelastic equations in modal coordinates

The vibration response (in terms of displacement) of a thin plate can be represented as a convergent series of the mass-normalized and orthogonal mode shapes, $\phi_{mn}(x,y)$, and generalized modal coordinates, $\eta_{mn}(t)$, such that

$$w(x,y,t) = \sum_{n=1}^{\infty} \sum_{m=1}^{\infty} \phi_{mn}(x,y) \eta_{mn}(t) \quad (5)$$

By following the standard modal analysis procedure, electromechanically coupled second-order differential equation for the generalized modal coordinate $\eta_{mn}(t)$ of the m th vibration mode can be obtained as

$$\frac{d^2 \eta_{mn}}{dt^2} + 2\zeta_{mn} \omega_{mn} \frac{d\eta_{mn}}{dt} + \omega_{mn}^2 \eta_{mn}(t) - \sum_{k=1}^K (\tilde{\theta}_{mn})_k v_k(t) = f_{mn}(t) \quad (6)$$

where ω_{mn} is the undamped natural frequency, ζ_{mn} is the modal damping ratio, and $f_{mn}(t)$ is the modal forcing term given by $f_{mn}(t) = f(t)\phi_{mn}(x_0,y_0)$. The electromechanical coupling term $\tilde{\theta}_{mn}^k$ for the k th uniform piezopatch in modal coordinates can be obtained as

$$\tilde{\theta}_{mn}^k = \theta_k \left[\int_{y_{k,1}}^{y_{k,2}} \frac{\partial \phi_{mn}(x,y)}{\partial x} \Big|_{x_{k,1}}^{x_{k,2}} dy + \int_{x_{k,1}}^{x_{k,2}} \frac{\partial \phi_{mn}(x,y)}{\partial y} \Big|_{y_{k,1}}^{y_{k,2}} dx \right] \quad (7)$$

By substituting equations (5) and (7) into equation (3), the current output is expressed in modal coordinates as

$$i_k(t) = - \sum_{n=1}^{\infty} \sum_{m=1}^{\infty} \frac{d\eta_{mn}(t)}{dt} \tilde{\theta}_{mn}^k \quad (8)$$

and the electrical circuit equation for the series connection can be written in modal coordinates as

$$(C_p)_k \frac{dv_k(t)}{dt} + \frac{v(t)}{R_l} + \sum_{n=1}^{\infty} \sum_{m=1}^{\infty} \frac{d\eta_{mn}(t)}{dt} \tilde{\theta}_{mn}^k = 0 \quad k = 1, 2, \dots, K \quad (9)$$

whereas the circuit equation of the parallel connection is

$$\frac{dv(t)}{dt} \sum_{k=1}^K (C_p)_k + \frac{v(t)}{R_l} + \sum_{k=1}^K \sum_{n=1}^{\infty} \sum_{m=1}^{\infty} \frac{d\eta_{mn}(t)}{dt} \tilde{\theta}_{mn}^k = 0 \quad (10)$$

in modal coordinates. Therefore, the electroelastic model for the series connection case in modal coordinates is due to equations (6) and (9), while equations (6) and (10) represent electroelastic model for the parallel connection case.

Harmonic excitation and electroelastic frequency response for the series connection case

If the transverse force excitation on the host plate is assumed to be harmonic of the form $f(t) = F_0 e^{j\omega t}$ (where F_0 is the force amplitude and ω is the excitation frequency), the linear system assumption implies that the mechanical and electrical responses can be represented as harmonic functions: $\eta_{mn}(t) = H_{mn}^s e^{j\omega t}$ and $v_k(t) = V_k e^{j\omega t}$, where H_{mn}^s and V_k are complex valued amplitudes and superscript s denotes the series connection of harvester patches. Substitution of these harmonic functions into equation (6) enables the extraction of H_{mn}^s as

$$H_{mn}^s = \frac{F_0 \phi_{mn}(x_0,y_0) + \theta_{mn}^T \mathbf{V}}{\omega_{mn}^2 - \omega^2 + j2\zeta_{mn} \omega_{mn} \omega} \quad (11)$$

where the individual voltage vector \mathbf{V} (with the dimensions of $K \times 1$) includes the voltage across each piezopatch harvester as $\mathbf{V} = [V_1 \ V_2 \ \dots \ V_K]^T$, and the electromechanical coupling vector $\boldsymbol{\theta}_{mn}$ (with the dimensions of $K \times 1$) is $\boldsymbol{\theta}_{mn} = [\tilde{\theta}_{mn}^1 \ \tilde{\theta}_{mn}^2 \ \dots \ \tilde{\theta}_{mn}^K]^T$, where superscript T stands for the transpose. The individual voltage vector \mathbf{V} can be then calculated by $\mathbf{V} = F_0 \mathbf{Q}^{-1} \mathbf{P}$, where \mathbf{Q} is a square matrix with the dimensions of $K \times K$ and \mathbf{P} is a column vector with the dimensions of $K \times 1$

$$\mathbf{Q} = \begin{bmatrix} \frac{1 + j\omega(C_p)_1 R_1}{R_1} + \sum_{n=1}^{\infty} \sum_{m=1}^{\infty} \frac{j\omega \tilde{\theta}_{mn}^1 \tilde{\theta}_{mn}^1}{\omega_{mn}^2 - \omega^2 + j2\zeta_{mn} \omega_{mn} \omega} & \dots & \frac{1}{R_1} + \sum_{n=1}^{\infty} \sum_{m=1}^{\infty} \frac{j\omega \tilde{\theta}_{mn}^1 \tilde{\theta}_{mn}^K}{\omega_{mn}^2 - \omega^2 + j2\zeta_{mn} \omega_{mn} \omega} \\ \vdots & \ddots & \vdots \\ \frac{1}{R_1} + \sum_{n=1}^{\infty} \sum_{m=1}^{\infty} \frac{j\omega \tilde{\theta}_{mn}^1 \tilde{\theta}_{mn}^K}{\omega_{mn}^2 - \omega^2 + j2\zeta_{mn} \omega_{mn} \omega} & \dots & \frac{1 + j\omega(C_p)_K R_1}{R_1} + \sum_{n=1}^{\infty} \sum_{m=1}^{\infty} \frac{j\omega \tilde{\theta}_{mn}^K \tilde{\theta}_{mn}^K}{\omega_{mn}^2 - \omega^2 + j2\zeta_{mn} \omega_{mn} \omega} \end{bmatrix} \quad (12)$$

$$\mathbf{P} = \begin{bmatrix} - \sum_{n=1}^{\infty} \sum_{m=1}^{\infty} \frac{j\omega \tilde{\theta}_{mn}^1 \phi_{mn}(x_0, y_0)}{\omega_{mn}^2 - \omega^2 + j2\zeta_{mn} \omega_{mn} \omega} \\ \vdots \\ - \sum_{n=1}^{\infty} \sum_{m=1}^{\infty} \frac{j\omega \tilde{\theta}_{mn}^K \phi_{mn}(x_0, y_0)}{\omega_{mn}^2 - \omega^2 + j2\zeta_{mn} \omega_{mn} \omega} \end{bmatrix} \quad (13)$$

The steady-state voltage output $v(t)$ across the load resistance can be calculated as

$$v(t) = \sum_{k=1}^K V_k e^{j\omega t} = \mathbf{u}^T F_0 \mathbf{Q}^{-1} \mathbf{P} e^{j\omega t} \quad (14)$$

where \mathbf{u} is a unit vector with the dimensions of $K \times 1$. After that, substitution of equation (14) into equations (5) and (11) yields the steady-state transverse vibration response (in terms of displacement) as

$$w(x, y, t) = \sum_{n=1}^{\infty} \sum_{m=1}^{\infty} \phi_{mn}(x, y) \frac{F_0 \phi_{mn}(x_0, y_0) + \boldsymbol{\theta}_{mn}^T F_0 \mathbf{Q}^{-1} \mathbf{P}}{\omega_{mn}^2 - \omega^2 + j2\zeta_{mn} \omega_{mn} \omega} e^{j\omega t} \quad (15)$$

Having the steady-state response of voltage output, the voltage FRF $\alpha^s(\omega)$ between the voltage output and force input can be extracted as

$$\alpha^s(\omega) = \frac{v(t)}{F_0 e^{j\omega t}} = \mathbf{u}^T \mathbf{Q}^{-1} \mathbf{P} \quad (16)$$

and the displacement FRF $\beta^s(x, y, \omega)$ between the displacement of the plate and force input is given by

$$\beta^s(x, y, \omega) = \frac{w(x, y, t)}{F_0 e^{j\omega t}} = \sum_{n=1}^{\infty} \sum_{m=1}^{\infty} \phi_{mn}(x, y) \frac{\phi_{mn}(x_0, y_0) + \boldsymbol{\theta}_{mn}^T \mathbf{Q}^{-1} \mathbf{P}}{\omega_{mn}^2 - \omega^2 + j2\zeta_{mn} \omega_{mn} \omega} \quad (17)$$

for the position (x, y) on the plate.

Harmonic excitation and electroelastic frequency response for the parallel connection case

Similar to the series connection case, when the transverse point force acting on the surface of the plate is

harmonic of the form $f(t) = F_0 e^{j\omega t}$, the mechanical and electrical responses can be assumed to be harmonic at the same frequency. Note that, for the parallel connection, the individual voltage output of each k th piezopatch harvester is equal to the voltage output $v(t)$ across the resistor. Substitution of harmonic functions into equation (6) enables extraction of H_{mn}^p as

$$H_{mn}^p = \frac{F_0 \phi_{mn}(x_0, y_0) + V \sum_{k=1}^K \tilde{\theta}_{mn}^k}{\omega_{mn}^2 - \omega^2 + j2\zeta_{mn} \omega_{mn} \omega} \quad (18)$$

and employing equation (18) in equation (10) yields the complex voltage amplitude V across the resistive load as

$$V = \frac{- \sum_{k=1}^K \sum_{n=1}^{\infty} \sum_{m=1}^{\infty} \frac{j\omega \tilde{\theta}_{mn}^k F_0 \phi_{mn}(x_0, y_0)}{\omega_{mn}^2 - \omega^2 + j2\zeta_{mn} \omega_{mn} \omega}}{j\omega \sum_{k=1}^K (C_p)_k + \frac{1}{R_1} + \sum_{k=1}^K \sum_{n=1}^{\infty} \sum_{m=1}^{\infty} \frac{j\omega \tilde{\theta}_{mn}^k \sum_{k=1}^K \tilde{\theta}_{mn}^k}{\omega_{mn}^2 - \omega^2 + j2\zeta_{mn} \omega_{mn} \omega}} \quad (19)$$

Then the steady-state vibration response of the plate at any position (x, y) and time t is

$$w(x, y, t) = \sum_{n=1}^{\infty} \sum_{m=1}^{\infty} \phi_{mn}(x, y) \frac{F_0 \phi_{mn}(x_0, y_0) + V \sum_{k=1}^K \tilde{\theta}_{mn}^k}{\omega_{mn}^2 - \omega^2 + j2\zeta_{mn} \omega_{mn} \omega} e^{j\omega t} \quad (20)$$

Therefore, the closed-form expression for the voltage FRF $\alpha^p(\omega)$ for the parallel connection case is

$$\alpha^p(\omega) = \frac{v(t)}{F_0 e^{j\omega t}} - \frac{\sum_{k=1}^K \sum_{n=1}^{\infty} \sum_{m=1}^{\infty} \frac{j\omega \tilde{\theta}_{mn}^k \phi_{mn}(x_0, y_0)}{\omega_{mn}^2 - \omega^2 + j2\zeta_{mn}\omega_{mn}\omega}}{j\omega \sum_{k=1}^K (C_p)_k + \frac{1}{R_l} + \sum_{k=1}^K \sum_{n=1}^{\infty} \sum_{m=1}^{\infty} \frac{j\omega \tilde{\theta}_{mn}^k \sum_{k=1}^K \tilde{\theta}_{mn}^k}{\omega_{mn}^2 - \omega^2 + j2\zeta_{mn}\omega_{mn}\omega}} \quad (21)$$

and the expression for the displacement FRF $\beta^p(x, y, \omega)$ is

$$\beta^p(x, y, \omega) = \frac{w(x, y, t)}{F_0 e^{j\omega t}} = \sum_{n=1}^{\infty} \sum_{m=1}^{\infty} \phi_{mn}(x, y) \frac{\phi_{mn}(x_0, y_0) + \alpha^p(\omega) \sum_{k=1}^K \tilde{\theta}_{mn}^k}{\omega_{mn}^2 - \omega^2 + j2\zeta_{mn}\omega_{mn}\omega} \quad (22)$$

Having covered the electroelastic model development and steady-state solutions to harmonic excitation, next we explore stationary random excitation of the plate.

Broadband and band-limited random excitations: analytical and numerical solutions

Frequency-domain analytical solution

Broadband random vibrations. If the stationary transverse point-force excitation $f(t)$ is assumed to be ideal Gaussian white noise excitation having a constant PSD value of S_0 over the entire frequency domain (to represent broadband excitation), the multi-mode solution for the mean power output (i.e. the expected value of the power output) across the resistive load R_l is given by

$$E[P(t)] = \int_{-\infty}^{\infty} \frac{S_0}{R_l} |\alpha(\omega)|^2 d\omega \quad (23)$$

which is based on $P(t) = v^2(t)/R_l$, and $\alpha(\omega)$ is the unified representation of the voltage FRF for the series and parallel connection cases and includes all vibration modes of the host plate in the broad frequency spectrum (within the limits of the modeling assumptions). Closed-form voltage FRFs are given by equations (16) and (21) for the series and parallel connection configurations, respectively. One can substitute the corresponding voltage FRF into equation (23) and compute the mean power output by carrying out integration over the broad frequency range.

Likewise, for the same ideal Gaussian white noise excitation, the multi-mode analytical solution for the mean-square vibration response at an arbitrary position (x, y) and time t is

$$E[w^2(x, y, t)] = \int_{-\infty}^{\infty} S_0 |\beta(x, y, \omega)|^2 d\omega \quad (24)$$

where $\beta(\omega)$ is the unified representation of the displacement FRF for the series and the parallel connection cases and provided by equations (17) and (22), respectively. Note that here (and in the following) the mean-square velocity response can be easily obtained by modifying the FRF (equations (17) or (22)) used in the integrand of equation (24) to give the velocity instead of displacement (Zhao and Erturk, 2013a).

Band-limited random vibrations. For the case of band-limited stationary random excitation over a frequency range $[0, \bar{\omega}]$ (with the PSD of $S_f(\omega)$ covering the frequency range $[-\bar{\omega}, \bar{\omega}]$), the mean power output can be computed by performing the integration

$$E[P(t)] = \int_{-\bar{\omega}}^{\bar{\omega}} \frac{S_f(\omega)}{R_l} |\alpha(\omega)|^2 d\omega \quad (25)$$

and the mean-square vibration response is

$$E[w^2(x, y, t)] = \int_{-\bar{\omega}}^{\bar{\omega}} S_f(\omega) |\beta(x \cdot y, \omega)|^2 d\omega \quad (26)$$

Here, one should ensure to include all vibration modes appearing in the frequency range dictated by the force PSD when calculating the voltage and displacement FRFs, $\alpha(\omega)$ and $\beta(\omega)$.

Fourier series-based time-domain numerical solution

If the time history of a stationary random force excitation over a time period T is described in a deterministic fashion using its Fourier series representation

$$f(t) \cong p_0 + \sum_{r=1}^S \left[p_r \cos\left(\frac{2\pi r t}{T}\right) + q_r \sin\left(\frac{2\pi r t}{T}\right) \right] \quad (27)$$

where S is the number of terms, p_0 is the mean value, while p_r and q_r are the Fourier coefficients (Zhao and Erturk, 2013a). The time history of the modal time response $\eta_{mn}(t)$ for the m th vibration mode over a time period T can be obtained by solving electroelastic differential equations in modal coordinates in the first-order form. The time histories of the voltage output and vibration response can be calculated over the same

time period T . Specifically, we consider random force excitation with zero mean value, that is, $p_0 = 0$ in equation (27). To this end, in the following, first-order representations of the electroelastic ordinary differential equations are presented for the series and parallel connection cases, and the expressions for the mean power output and mean-square vibration response are given.

First-order electroelastic equations for series connection. Electroelastic variables for the m th vibration mode can be obtained using equations (6) and (9) in the same vein as Erturk and Inman (2011)

$$u_{mn}^{(1)} = \eta_{mn}(t) \quad u_{mn}^{(2)} = \dot{\eta}_{mn}(t) \quad u^{(k+2)} = v_k(t) \quad (28)$$

where $k = 1, 2, \dots, K$

Here, $u_{mn}^{(1)}$ is the modal displacement, $u_{mn}^{(2)}$ is the modal velocity, and $u^{(k+2)}$ is the individual voltage output of the k th piezopatch. By introducing the foregoing variables into the electroelastic model given by equations (6) and (9), $2MN + K$ number of first-order differential equations are obtained as follows

$$\begin{bmatrix} \dot{u}_{11}^{(1)} & \dot{u}_{21}^{(1)} & \dots & \dot{u}_{MN}^{(1)} & \dot{u}_{11}^{(2)} & \dot{u}_{21}^{(2)} & \dots & \dot{u}_{MN}^{(2)} & \dot{u}^{(3)} & \dots & \dot{u}^{(K+2)} \end{bmatrix}^T = \begin{bmatrix} u_{11}^{(2)} \\ u_{21}^{(2)} \\ \vdots \\ u_{MN}^{(2)} \\ -2\zeta_{11}\omega_{11}u_{11}^{(2)} - \omega_{11}^2u_{11}^{(1)} + (\tilde{\theta}_{11}^1u^{(3)} + \tilde{\theta}_{11}^2u^{(4)} + \dots + \tilde{\theta}_{11}^Ku^{(K+2)}) + f_{11}(t) \\ -2\zeta_{21}\omega_{21}u_{21}^{(2)} - \omega_{21}^2u_{21}^{(1)} + (\tilde{\theta}_{21}^1u^{(3)} + \tilde{\theta}_{21}^2u^{(4)} + \dots + \tilde{\theta}_{21}^Ku^{(K+2)}) + f_{21}(t) \\ \vdots \\ -2\zeta_{MN}\omega_{MN}u_{MN}^{(2)} - \omega_{MN}^2u_{MN}^{(1)} + (\tilde{\theta}_{MN}^1u^{(3)} + \tilde{\theta}_{MN}^2u^{(4)} + \dots + \tilde{\theta}_{MN}^Ku^{(K+2)}) + f_{MN}(t) \\ \frac{-1}{(C_p)_1} \left[\frac{1}{R_1}(u^{(3)} + u^{(4)} + \dots + u^{(K+2)}) + (\tilde{\theta}_{11}^1u_{11}^{(2)} + \tilde{\theta}_{21}^1u_{21}^{(2)} + \dots + \tilde{\theta}_{MN}^1u_{MN}^{(2)}) \right] \\ \vdots \\ \frac{-1}{(C_p)_K} \left[\frac{1}{R_1}(u^{(3)} + u^{(4)} + \dots + u^{(K+2)}) + (\tilde{\theta}_{11}^Ku_{11}^{(2)} + \tilde{\theta}_{21}^Ku_{21}^{(2)} + \dots + \tilde{\theta}_{MN}^Ku_{MN}^{(2)}) \right] \end{bmatrix} \quad (29)$$

where $f_{mn}(t)$ is the transverse random point-force excitation in modal coordinates. Zero initial conditions will be assumed in the simulations of this article.

Solving equations (29) using an ordinary differential equation (ODE) solver (e.g. explicit Runge–Kutta method), the time histories of electroelastic states (i.e. modal time responses and voltage output) can be obtained. After that, the vibration response (in terms of velocity) can be approximated as a finite series of the eigenfunctions and modal time responses as

$$\begin{aligned} \dot{w}(x, y, t) &\cong \sum_{n=1}^N \sum_{m=1}^M \phi_{mn} \dot{\eta}_{mn} \\ &= \phi_{11} \dot{\eta}_{11} + \phi_{21} \dot{\eta}_{21} + \phi_{12} \dot{\eta}_{12} + \dots + \phi_{MN} \dot{\eta}_{MN} \end{aligned} \quad (30)$$

by truncating the computation of the modal time responses at M number of modes along the x -axis and N number of modes along the y -axis. Once again, the number of modes to take depends on the frequency spectrum of the force signal. The mean-square velocity response can then be computed using

$$E[\dot{w}^2(x, y, t)] = \frac{1}{T} \int_0^T \dot{w}^2(x, y, t) dt = \sigma_{\dot{w}}^2 \quad (31)$$

where $\sigma_{\dot{w}}$ is the standard deviation (root mean square) of the velocity of the plate at positions x and y . The voltage output across the resistive load is

$$v(t) = \sum_{k=1}^K v_k = \sum_{k=1}^K u^{k+2} \quad (32)$$

and the mean power output can be obtained using

$$E[P(t)] = \frac{1}{T} \int_0^T \frac{v^2(t)}{R_1} dt = \frac{\sigma_v^2}{R_1} \quad (33)$$

where σ_v is the standard deviation (root mean square) of the voltage output across the resistor.

First-order electroelastic equations for parallel connection. Similarly, the electroelastic variables for the parallel connection can be extracted from equations (6) and (10) for the mn th vibration mode as

$$u_{mn}^{(1)} = \eta_{mn}(t) \quad u_{mn}^{(2)} = \dot{\eta}_{mn}(t) \quad u^{(3)} = v(t) \quad (34)$$

where $u_{mn}^{(1)}$ is the modal displacement coordinate, $u_{mn}^{(2)}$ is the modal velocity coordinate, and $u^{(3)}$ is the voltage output across the resistive load. By introducing the electroelastic state variables into the governing electroelastic equations given by equations (6) and (10), $2MN + 1$ number of first-order differential equations are obtained for the electroelastic states as

$$\begin{bmatrix} \dot{u}_{11}^{(1)} & \dot{u}_{21}^{(1)} & \dots & \dot{u}_{MN}^{(1)} & \dot{u}_{11}^{(2)} & \dot{u}_{21}^{(2)} & \dots & \dot{u}_{MN}^{(2)} & \dot{u}^{(3)} \end{bmatrix}^T = \begin{bmatrix} u_{11}^{(2)} \\ u_{21}^{(2)} \\ \vdots \\ u_{MN}^{(2)} \\ -2\zeta_{11}\omega_{11}u_{11}^{(2)} - \omega_{11}^2u_{11}^{(1)} + (\tilde{\theta}_{11}^1 + \tilde{\theta}_{11}^2 + \dots + \tilde{\theta}_{11}^K)u^{(3)} + f_{11}(t) \\ -2\zeta_{21}\omega_{21}u_{21}^{(2)} - \omega_{21}^2u_{21}^{(1)} + (\tilde{\theta}_{21}^1 + \tilde{\theta}_{21}^2 + \dots + \tilde{\theta}_{21}^K)u^{(3)} + f_{21}(t) \\ \vdots \\ -2\zeta_{MN}\omega_{MN}u_{MN}^{(2)} - \omega_{MN}^2u_{MN}^{(1)} + (\tilde{\theta}_{MN}^1 + \tilde{\theta}_{MN}^2 + \dots + \tilde{\theta}_{MN}^K)u^{(3)} + f_{MN}(t) \\ \frac{-1}{(C_p)_1 + \dots + (C_p)_K} \left\{ \frac{u^{(3)}}{R_1} + \begin{bmatrix} u_{11}^{(2)}(\tilde{\theta}_{11}^1 + \tilde{\theta}_{11}^2 + \dots + \tilde{\theta}_{11}^K) + \\ u_{21}^{(2)}(\tilde{\theta}_{21}^1 + \tilde{\theta}_{21}^2 + \dots + \tilde{\theta}_{21}^K) + \dots + \\ u_{MN}^{(2)}(\tilde{\theta}_{MN}^1 + \tilde{\theta}_{MN}^2 + \dots + \tilde{\theta}_{MN}^K) \end{bmatrix} \right\} \end{bmatrix} \quad (35)$$

Therefore, by numerically solving these electroelastic equations using the time history of the random force excitation over a time period T , the voltage output across the resistive load, $v(t) = u^{(3)}$, is obtained. The mean-square vibration response and the mean power can be calculated as in the series configuration case given by equations (31) and (33).

Experimental validations

Experimental setup and piezopatch energy harvesters

The experimental setup used for frequency and time measurements is presented in Figure 3. A fully clamped aluminum plate is used as the host plate. Three electroded piezoceramic patches (T105-A4E-602 by Piezo Systems, Inc.) are employed as piezopatch energy harvesters by attaching them on the plate. The geometric

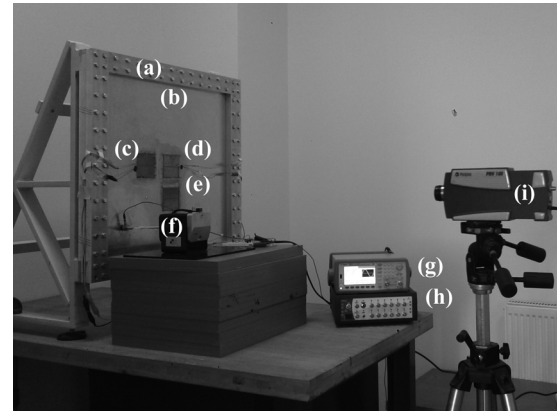


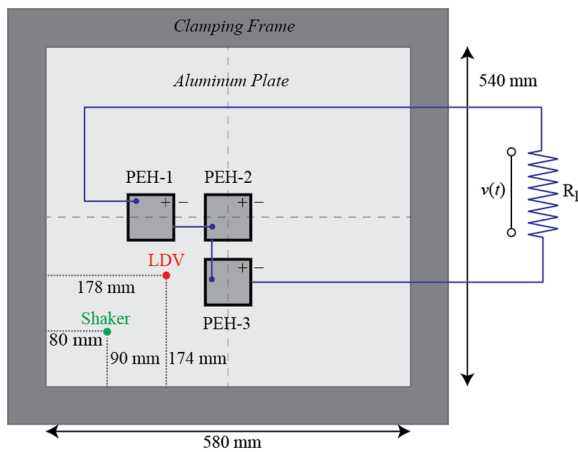
Figure 3. Experimental setup: (a) clamping frame, (b) aluminum plate, (c) PEH-I, (d) PEH-II, (e) PEH-III, (f) modal shaker, (g) signal generator, (h) signal analyzer, and (i) laser vibrometer.

and material properties of the aluminum plate and the piezopatches are given in Table 1. The three piezopatch harvesters (labeled as PEH-1, PEH-2, and PEH-3) having identical polarities are perfectly bonded on the surface of the plate as shown in Figures 3 and 4. The bottom (negative) and top (positive) surfaces of the piezopatch harvesters are covered by thin vacuum sputtered nickel electrodes of negligible thickness (by the manufacturer) and the bonding areas on the aluminum plate are electrically insulated with 3M Scotch 1601 spray.

Series connection of the three piezopatch harvesters is employed throughout the experiments by connecting the bottom and top electrodes sequentially. The electrical load (i.e. simply a resistor) is then connected to the resultant terminals as illustrated in Figure 4. A modal shaker is used to excite the plate. The attachment point of the shaker's stinger rod can be seen in both Figures 3

Table 1. Geometric, material, and electroelastic properties.

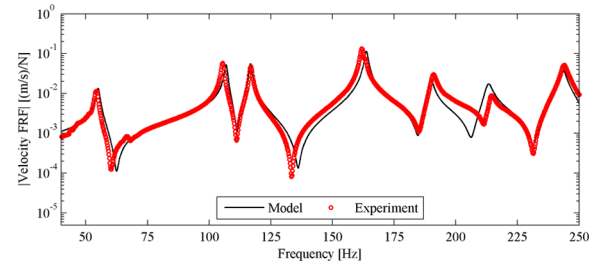
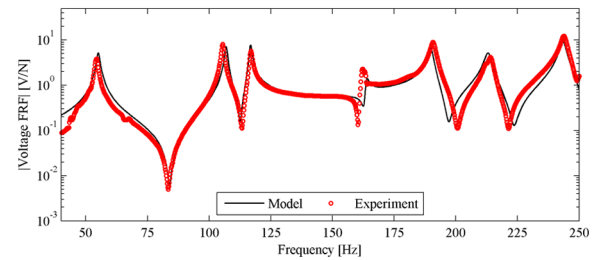
Property	Aluminum	Piezoceramic patch
Length (mm)	580	72.4
Width (mm)	540	72.4
Thickness (mm)	1.9	0.267
Young's modulus (GPa)	65.1	66
Mass density (kg/m^3)	2575	7800
Piezoelectric constant d_{31} (pm/V)	–	–190
Permittivity constant ϵ_{33}^S (nF/m)	–	10.38

**Figure 4.** Series connection configuration of piezopatch energy harvesters attached on the thin aluminum plate and the locations of LDV target and shaker attachment point.

and 4. The applied force is monitored by placing a force transducer (PCB 208C01) between the shaker's armature and the plate surface. A laser Doppler vibrometer (LDV—Polytec PDV 100) is used to measure the transverse velocity of the plate at the target point shown in Figure 4. The signals obtained from the force transducer, the laser vibrometer, and the voltage across the resistive load are sent to the data acquisition system for time-domain and frequency response analyses.

Experimental and analytical electroelastic FRFs

Before carrying out random vibration experiments, sine-sweep tests are conducted and experimental FRFs are compared with analytical predictions to demonstrate the accuracy of the electroelastic model in frequency domain with a focus on the first seven vibration modes. Using the experimental setup shown in Figure 3, the velocity FRF (i.e. velocity response per force input) and the voltage FRF (i.e. voltage output per force input) are obtained from the signal analyzer by exciting the plate with a modal shaker (as in Figures 3 and 4). Figure 5 presents the experimental and analytical velocity FRFs for a resistive load of $1 \text{ M}\Omega$ (close

**Figure 5.** Comparison of the experimental and analytical velocity FRFs for a resistive load of $1 \text{ M}\Omega$.**Figure 6.** Comparison of the experimental and analytical voltage FRFs for a resistive load of $1 \text{ M}\Omega$.

to open-circuit conditions). It can be seen from this figure that the analytical velocity FRF accurately predicts the experimental velocity FRF measurement near resonance and anti-resonance frequencies up to 250 Hz. Note that the modal damping ratios used for the analytical predictions are identified from the experimental velocity FRF using the half-power point method. The experimental measurements and analytical predictions of the voltage FRF are given for a resistive load of $1 \text{ M}\Omega$ in Figure 6. The analytical voltage FRF is in very good agreement with the experimental data. It is important to note that at higher modes, there is minor amplitude-wise and frequency-wise mismatch between the analytical predictions and experimental data points, which may be related to the bonding and positioning imperfections of piezopatch harvesters, clamping imperfections of the plate, and unmodeled effects. Overall, the analytical and experiment results agree reasonably well for both the velocity and the voltage FRFs. Therefore, it can be concluded that the electroelastic model developed in this work can be used to predict the vibration and velocity responses with good accuracy in the bandwidth up to 250 Hz.

Experimental random excitation

Random vibration experiments are carried out by exciting the plate with a random force through the modal shaker using the configuration shown in Figures 3 and 4. In the experiments, the force input, the voltage across the resistor, and the transverse velocity of the

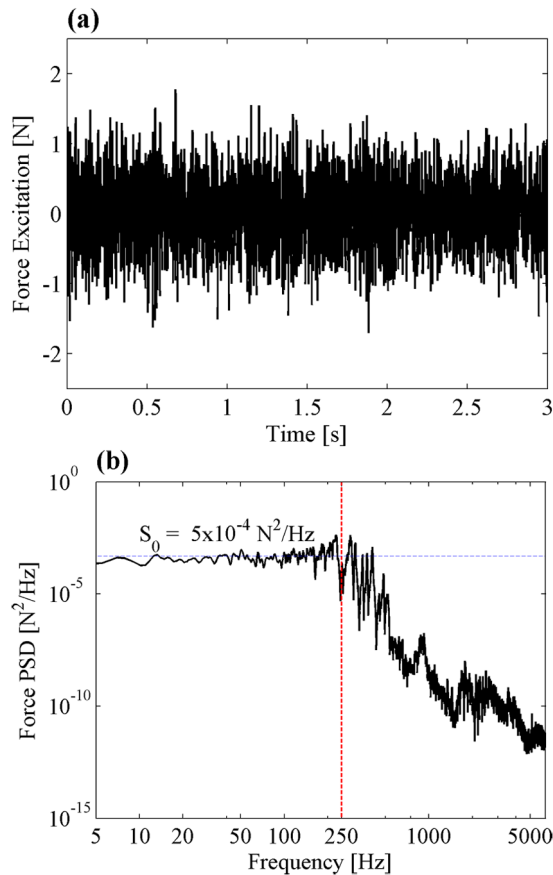


Figure 7. (a) A sample time history of the measured random point force and (b) its PSD.

plate are measured and recorded by using the signal analyzer. The excitation signal driving the modal shaker is a band-limited noise produced by the signal generator. Figure 7 presents a sample time history of the force input and its PSD. The sampling frequency is set to 12.8 kHz; therefore, the PSD is presented until 6400 Hz. It can be seen that the PSD of the excitation signal is reasonably flat up to 250 Hz, which covers the range used in frequency response validation in the previous section. The standard deviation of the force input in Figure 7(a) is computed to be 0.473 N from time history and the average value of flat portion of PSD is read from Figure 7(b) as approximately $S_0 = 5 \times 10^{-4} \text{ N}^2/\text{Hz}$. Note that Figure 7(a) is not an ideal band-limited signal (as clear from its PSD) due to experimental imperfections, yet it is a reasonable approximation for model validation purpose.

Resistor sweep experiments are then performed for 14 resistive loads ranging from 500 Ω (close to short-circuit conditions) to 1 M Ω (close to open-circuit conditions). For each resistive load, the experimental measurement is repeated five times and each measurement is taken for 3 s. Therefore, 70 different time series with total time duration of 210 s (in each case) are recorded and their PSD profiles are obtained. For each measurement of each resistor test, Figure 8 presents the standard deviations of time signals

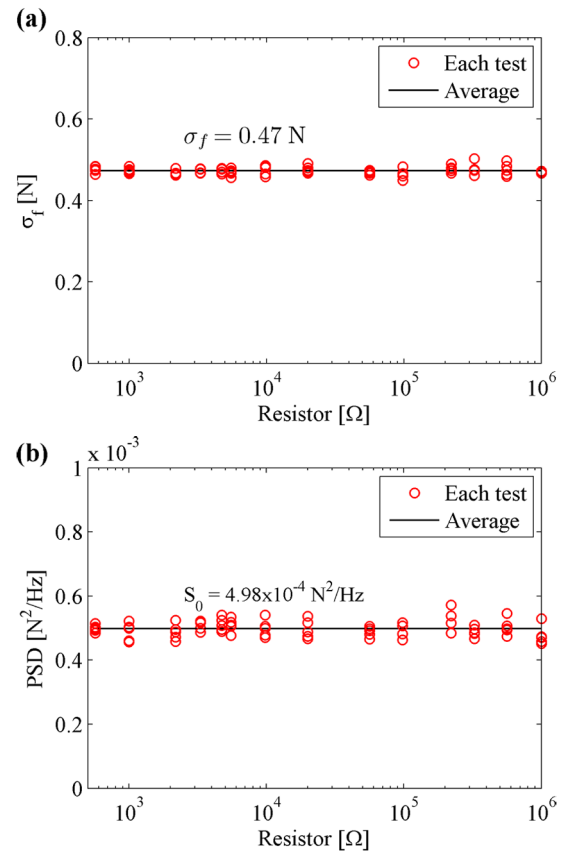


Figure 8. Comparison of resistor sweep tests in terms of (a) standard deviations and (b) PSD values.

and average PSD levels. This comparison suggests that the excitation signal provided by the modal shaker can indeed be approximated as a stationary-ergodic process in agreement with the modeling assumptions.

Mean power output and mean-square velocity response

The experimental measurements for the mean power output and mean-square velocity responses are presented along with the analytical and numerical predictions in Figure 9. It can be observed that the numerical and analytical predictions agree well with the experimental data points for a wide range of resistive loads. For the frequency-domain solution process, the mean power and mean-square velocity responses are calculated using equations (25) and (26). The frequency-dependent PSD is obtained from the first experimental measurement (i.e. the first measurement of a resistive load of 1 M Ω). The upper frequency limit ($\bar{\omega}$) of the frequency-domain integration is set to 250 Hz due to Figure 7(b). In order to obtain numerical predictions of the mean power output and the mean-square vibration responses, an explicit fourth-order Runge–Kutta algorithm is used to solve the first-order electroelastic

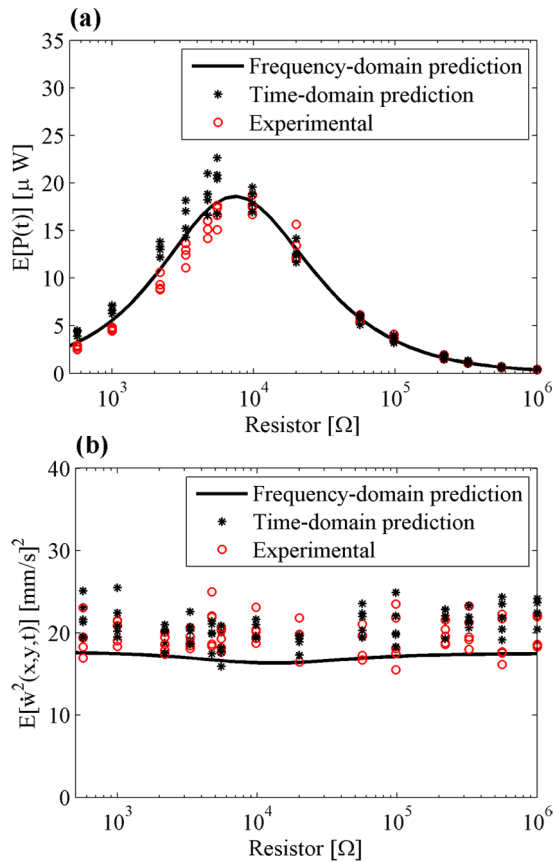


Figure 9. Comparison of the experimental measurements with frequency-domain and time-domain simulations for a set of resistive loads: (a) mean power output and (b) mean-square velocity response.

equations under Fourier series-based excitation. Time-domain simulations are performed with the individual time histories of force inputs for all 70 experimental measurements (five tests for each one of the 14 resistors) using the first-order differential equations given by equation (29). As can be seen in Figure 9, five different data points at each resistor are presented for the experimental measurements and time-domain predictions. Figure 10 presents the average of these five separate values at each resistor with error bars, indicating the deviations of five repeated measurements. It can be seen that the measurement deviations of mean power output are wider around the optimum resistive loads, where more power output is extracted compared to the neighborhoods of short- and open-circuit conditions. It can also be observed from Figure 10(b) that there are amplitude-wise differences between the model predictions and experimental results for the vibration response. This mismatch might be due to the sensitivity of the velocity measurement to the orientation of the laser vibrometer and mounting of the shaker armature. Part of the error in Figures 9 and 10 can be attributed to non-ideal nature of band-limited random excitation in the experiments (i.e. Figure 7 is not an ideal band-limited excitation but is more in the form

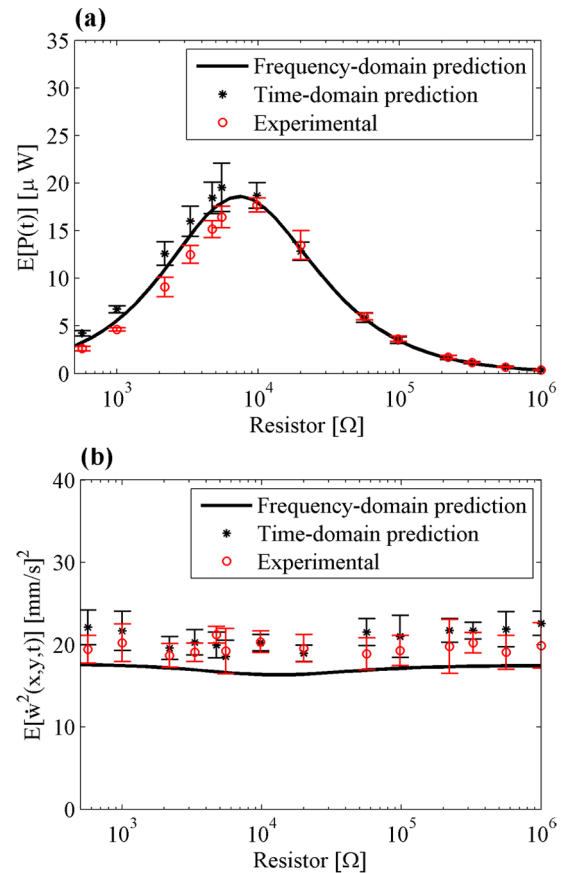


Figure 10. Comparison of the average experimental measurements with frequency-domain and average time-domain simulations for a set of resistive loads: (a) mean power output and (b) mean-square velocity response.

of a first-order low-pass filtered white noise). Overall, the model predictions are in very good agreement with the electromechanical system response.

Conclusion

A structurally integrated piezopatch harvester is a practical alternative to piezoelectric resonant cantilever beam arrangements especially for light-weight, thin, and two-dimensional structures. Furthermore, multiple piezopatch harvesters connected in series and/or parallel can enhance both the electrical power output and the frequency bandwidth. In this article, electroelastic modeling and experimental investigations of multiple piezopatch-based energy harvesting from broadband and band-limited random vibrations of a thin plate are studied. Electroelastic models for the series and parallel connection configurations of piezopatches are obtained and closed-form expressions for the electroelastic FRFs are presented. For stationary random vibration of the host plate, frequency-domain and time-domain solutions are obtained for the mean power output and mean-square vibration response. The frequency-domain analytical solution is expressed in terms of electroelastic

FRFs and PSD of random force excitation, while the time-domain numerical solutions of mean power output and mean-square vibration response are given by representing electroelastic model in the first-order form and the excitation in a deterministic Fourier series representation. Therefore, if the PSD of random force excitation is known, the frequency-domain solution can be used to predict the expected values of the structural and electrical responses. Alternatively, one can also find the expected values of the responses using time-domain numerical solutions for a given time history. It is important to take sufficient number of structural modes in the distributed-parameter solution based on the frequency bandwidth of random excitation. The experiments for random vibration energy harvesting are performed with the experimental setup having triple piezopatch harvesters connected in series. After verifying the stationary nature of the experimental excitation, it is shown that the analytical and numerical predictions of random structural and electrical responses agree well with the experimental measurements for a wide range of resistive load values. The electroelastic modeling approach and the formulation for the stochastic power output presented by this article can be used for optimal positioning of the harvester patches on thin plate structures for energy harvesting from stationary random vibration.

Declaration of Conflicting Interests

The author(s) declared no potential conflicts of interest with respect to the research, authorship, and/or publication of this article.

Funding

The author(s) disclosed receipt of the following financial support for the research, authorship, and/or publication of this article: This study was supported by the Koç University TÜPRAŞ Energy Center (KUTEM).

References

- Adhikari S, Friswell MI and Inman DJ (2009) Piezoelectric energy harvesting from broadband random vibrations. *Smart Materials and Structures* 18: 115005.
- Anton SR and Sodano HA (2007) A review of power harvesting using piezoelectric materials (2003–2006). *Smart Materials and Structures* 16: R1–R21.
- Aridogan U, Basdogan I and Erturk A (2014a) Analytical modeling and experimental validation of a structurally integrated piezoelectric energy harvester on a thin plate. *Smart Materials and Structures* 23: 045039.
- Aridogan U, Basdogan I and Erturk A (2014b) Multiple patch-based broadband piezoelectric energy harvesting on plate-based structures. *Journal of Intelligent Material Systems and Structures* 25: 1664–1680.
- Barton DAW, Burrow SG and Clare LR (2010) Energy harvesting from vibrations with a nonlinear oscillator. *Journal of Vibration and Acoustics* 132: 021009.
- Beeby SP, Torah RN, Tudor MJ, et al. (2007) A micro electromagnetic generator for vibration energy harvesting. *Journal of Micromechanics and Microengineering* 17: 1257–1265.
- Beeby SP, Tudor MJ and White NM (2006) Energy harvesting vibration sources for microsystems applications. *Measurement Science and Technology* 17: R175–R195.
- Behrens S, Fleming AJ and Moheimani SOR (2003) A broadband controller for shunt piezoelectric damping of structural vibration. *Smart Materials and Structures* 12: 18–28.
- Blystad LCJ, Halvorsen E and Husa S (2010) Piezoelectric MEMS energy harvesting systems driven by harmonic and random vibrations. *IEEE Transactions on Ultrasonics, Ferroelectrics and Frequency Control* 57: 908–919.
- Casadei F, Dozio L, Ruzzene M, et al. (2010) Periodic shunted arrays for the control of noise radiation in an enclosure. *Journal of Sound and Vibration* 329: 3632–3646.
- Cook-Chennault KA, Thambi N and Sastry AM (2008) Powering MEMS portable devices—a review of non-regenerative and regenerative power supply systems with special emphasis on piezoelectric energy harvesting systems. *Smart Materials and Structures* 17: 043001.
- Daqaq MF (2010) Response of uni-modal Duffing-type harvesters to random forced excitations. *Journal of Sound and Vibration* 329: 3621–3631.
- Daqaq MF (2011) Transduction of a bistable inductive generator driven by white and exponentially correlated Gaussian noise. *Journal of Sound and Vibration* 330: 2554–2564.
- De Marqui C and Erturk A (2012) Electroaeroelastic analysis of airfoil-based wind energy harvesting using piezoelectric transduction and electromagnetic induction. *Journal of Intelligent Material Systems and Structures* 24: 846–854.
- De Marqui C, Erturk A and Inman DJ (2009) An electromechanical finite element model for piezoelectric energy harvester plates. *Journal of Sound and Vibration* 327: 9–25.
- De Marqui C, Vieira WGR, Erturk A, et al. (2011) Modeling and analysis of piezoelectric energy harvesting from aeroelastic vibrations using the doublet-lattice method. *Journal of Vibration and Acoustics* 133: 011003.
- Elliott SJ and Zilletti M (2014) Scaling of electromagnetic transducers for shunt damping and energy harvesting. *Journal of Sound and Vibration* 333: 2185–2195.
- Elvin NG and Elvin AA (2009) A coupled finite element—circuit simulation model for analyzing piezoelectric energy generators. *Journal of Intelligent Material Systems and Structures* 20: 587–595.
- Erturk A (2012) Assumed-modes modeling of piezoelectric energy harvesters: Euler–Bernoulli, Rayleigh, and Timoshenko models with axial deformations. *Computers & Structures* 106: 214–227.
- Erturk A and Inman DJ (2008) A distributed parameter electromechanical model for cantilevered piezoelectric energy harvesters. *Journal of Vibration and Acoustics* 130: 041002-1–041002-15.
- Erturk A and Inman DJ (2009) An experimentally validated bimorph cantilever model for piezoelectric energy harvesting from base excitations. *Smart Materials and Structures* 18: 025009.
- Erturk A and Inman DJ (2011) *Piezoelectric Energy Harvesting*. Chichester: John Wiley & Sons.
- Erturk A, Renno JM and Inman DJ (2009) Modeling of piezoelectric energy harvesting from an L-shaped

- beam-mass structure with an application to UAVs. *Journal of Intelligent Material Systems and Structures* 20: 529–544.
- Ferrari M, Ferrari V, Guizzetti M, et al. (2008) Piezoelectric multifrequency energy converter for power harvesting in autonomous microsystems. *Sensors and Actuators A: Physical* 142: 329–335.
- Ferrari M, Ferrari V, Guizzetti M, et al. (2009) Improved energy harvesting from wideband vibrations by nonlinear piezoelectric converters. *Procedia Chemistry* 1: 1203–1206.
- Friswell MI and Adhikari S (2010) Sensor shape design for piezoelectric cantilever beams to harvest vibration energy. *Journal of Applied Physics* 108: 014901–014906.
- Harne RL (2012) Concurrent attenuation of, and energy harvesting from, surface vibrations: experimental verification and model validation. *Smart Materials and Structures* 21: 035016.
- Harne RL (2013) Development and testing of a dynamic absorber with corrugated piezoelectric spring for vibration control and energy harvesting applications. *Mechanical Systems and Signal Processing* 36: 604–617.
- Harne RL and Fuller CR (2012) Modeling of a distributed device for simultaneous reactive vibration suppression and energy harvesting. *Journal of Intelligent Material Systems and Structures* 23: 655–664.
- Huan X, Yuantai H and Qing-Ming W (2008) Broadband piezoelectric energy harvesting devices using multiple bimorphs with different operating frequencies. *IEEE Transactions on Ultrasonics, Ferroelectrics and Frequency Control* 55: 2104–2108.
- Huang S-C and Lin K-A (2012) A novel design of a map-tuning piezoelectric vibration energy harvester. *Smart Materials and Structures* 21: 085014.
- Kim J and Jung Y-C (2006) Broadband noise reduction of piezoelectric smart panel featuring negative-capacitive-converter shunt circuit. *Journal of the Acoustical Society of America* 120: 2017–2025.
- Kim J and Kim J-H (2004) Multimode shunt damping of piezoelectric smart panel for noise reduction. *Journal of the Acoustical Society of America* 116: 942–948.
- Kim S-J and Kwak MK (2004) The nonlinear behaviour of a piezoelectric wafer: constitutive equations and simulation. *Smart Materials and Structures* 13: 184.
- Koshigoe S and Murdock JW (1993) A unified analysis of both active and passive damping for a plate with piezoelectric transducers. *Journal of the Acoustical Society of America* 93: 346–355.
- Kumar P, Narayanan S, Adhikari S, et al. (2014) Fokker–Planck equation analysis of randomly excited nonlinear energy harvester. *Journal of Sound and Vibration* 333: 2040–2053.
- Lallart M, Harari S, Petit L, et al. (2009) Blind switch damping (BSD): a self-adaptive semi-active damping technique. *Journal of Sound and Vibration* 328: 29–41.
- Lee C, Lim YM, Yang B, et al. (2009) Theoretical comparison of the energy harvesting capability among various electrostatic mechanisms from structure aspect. *Sensors and Actuators A: Physical* 156: 208–216.
- Lee S and Youn BD (2011) A new piezoelectric energy harvesting design concept: multimodal energy harvesting skin. *IEEE Transactions on Ultrasonics, Ferroelectrics and Frequency Control* 58: 629–645.
- Lien IC and Shu YC (2012) Array of piezoelectric energy harvesting by the equivalent impedance approach. *Smart Materials and Structures* 21: 082001.
- Litak G, Friswell MI and Adhikari S (2010) Magnetopiezoelectric energy harvesting driven by random excitations. *Applied Physics Letters* 96: 214103.
- Makihara K, Takeuchi S, Shimose S, et al. (2012) Innovative digital self-powered autonomous system for multimodal vibration suppression. *AIAA Journal* 50: 2004–2011.
- Moheimani SOR (2003) A survey of recent innovations in vibration damping and control using shunted piezoelectric transducers. *IEEE Transactions on Control Systems Technology* 11: 482–494.
- Moheimani SOR and Behrens S (2004) Multimode piezoelectric shunt damping with a highly resonant impedance. *IEEE Transactions on Control Systems Technology* 12: 484–491.
- Niederberger D, Fleming A, Moheimani SOR, et al. (2004) Adaptive multi-mode resonant piezoelectric shunt damping. *Smart Materials and Structures* 13: 1025.
- Ramlan R, Brennan M, Mace B, et al. (2010) Potential benefits of a non-linear stiffness in an energy harvesting device. *Nonlinear Dynamics* 59: 545–558.
- Rupp CJ, Evgrafov A, Maute K, et al. (2009) Design of piezoelectric energy harvesting systems: a topology optimization approach based on multilayer plates and shells. *Journal of Intelligent Material Systems and Structures* 20: 1923–1939.
- Saravanos DA (1999) Damped vibration of composite plates with passive piezoelectric-resistor elements. *Journal of Sound and Vibration* 221: 867–885.
- Scruggs JT (2009) An optimal stochastic control theory for distributed energy harvesting networks. *Journal of Sound and Vibration* 320: 707–725.
- Takeuchi S, Makihara K and Onoda J (2012) Reliable and evolvable vibration suppression by self-powered digital vibration control. *Journal of Vibration and Acoustics* 134: 024502–024504.
- Tang L, Yang Y and Soh CK (2010) Toward broadband vibration-based energy harvesting. *Journal of Intelligent Material Systems and Structures* 21: 1867–1897.
- Tiwari R and Kim KJ (2013) IPMC as a mechanoelectric energy harvester: tailored properties. *Smart Materials and Structures* 22: 015017.
- Tvedt LGW, Nguyen DS and Halvorsen E (2010) Nonlinear behavior of an electrostatic energy harvester under wide- and narrowband excitation. *Journal of Microelectromechanical Systems* 19: 305–316.
- Wang L and Yuan FG (2008) Vibration energy harvesting by magnetostrictive material. *Smart Materials and Structures* 17: 045009.
- Yang Y and Tang L (2009) Equivalent circuit modeling of piezoelectric energy harvesters. *Journal of Intelligent Material Systems and Structures* 20: 2223–2235.
- Zhao S and Erturk A (2013a) Electroelastic modeling and experimental validations of piezoelectric energy harvesting from broadband random vibrations of cantilevered bimorphs. *Smart Materials and Structures* 22: 015002.
- Zhao S and Erturk A (2013b) On the stochastic excitation of monostable and bistable electroelastic power generators: relative advantages and tradeoffs in a physical system. *Applied Physics Letters* 102: 103902.